Numerical investigation and simple modelling of the modulation of SSH and SWH altimetric estimates by wave groups

G. MONNIER, B. CAMUS…

DRAFT

1. *Introduction*

The power spectral density of ocean elevation, as measured by conventional radar altimeters (PLRM), is known to exhibit a “bump” near 0.1 cpkm, strongly departing from the oceanic spectral slope observed a lower wavenumber. Wave groups are suspected to contribute to this bump, essentially through modulation of the local surface height variance (or SWH). This hypothesis is supported by the fact that even baseline simulations of altimetric measurement, performed with homogeneous gaussian sea surfaces, exhibit similar spectral shape in the vicinity of the bump cutoff. In such simulations, only the variations of the waves envelope (responsible for wave groups) is intended to cover this frequency domain.

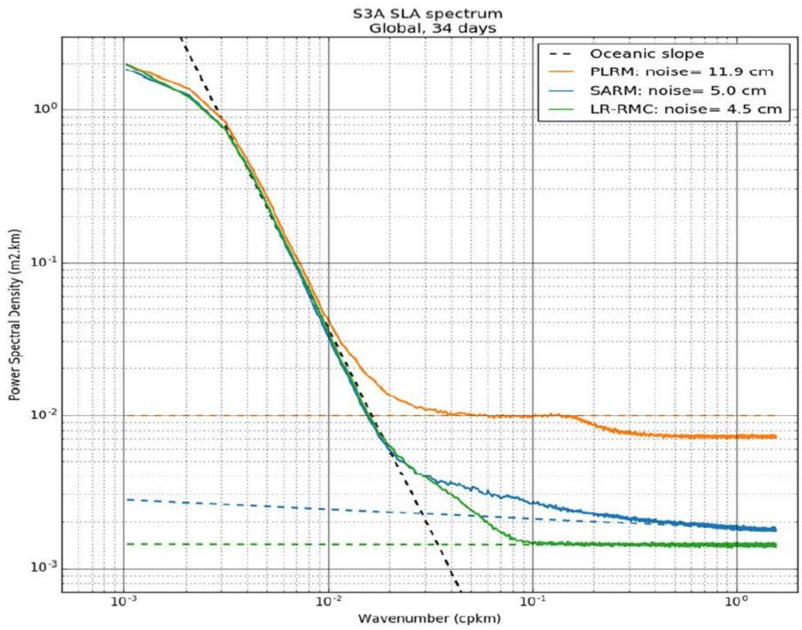

Figure 1 Average power spectral densities of the surface height typically observed in various altimetry modes

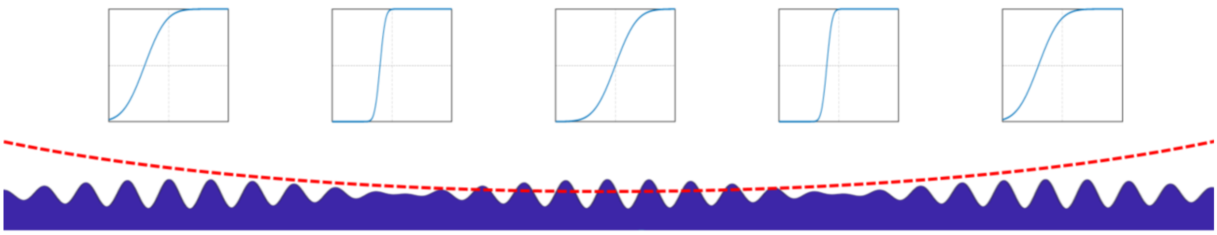

Figure 2 : view of the main ingredients of the considered model

The effect considered hereafter is illustrated in Figure 1. The "local" SWH is modulated along the x axis. We suppose that the measured altimetric profile can be described as a weighted average of the profiles that would be obtained in narrow bands orthogonal to x, in which SWH can be considered constant. The steepness of the profiles varies along x following SWH variations, while the average epoch at mid-height decreases as x^2, due to wave-front curvature. The SWH at the center and at the edges of the footprint dominate respectively the lower and upper sides of the profile slope. It can thus be expected that a harmonic variation of the SWH result in an asymmetric ascending front, possibly affecting the epoch. Furthermore, the maximum asymmetry should be obtained when the wavelength of the SWH modulation is comparable to the horizontal length encompassed by the ascending front, thus:

$$\lambda_{SWH} \sim \sqrt{2Z_{sat}SWH} \tag{0}$$

Where λ_{SWH} is the wavelength of the SWH modulation and Z_{sat} the satellite altitude. For $Z_{sat} = 800\ km$, and $SWH = 1 - 4\ m$, this very crude estimate gives a "resonant" frequency in the range $0.2 - 0.4\ cpkm$, which is not incompatible with the location of the spectral bump. This is a first clue in favor to the considered hypothesis, provided SWH modulations do exist in this wavenumber interval. As we shall see, wave groups provide such modulation, up to even higher wavenumbers.

In the following, a simple semi-analytic model is derived in an attempt to get a more quantitative view of the shape and magnitude of the expected spectral bump. It is then compared to spectra obtained through numerical simulation.

We propose hereafter a simple model, designed as the "minimum model" necessary to implement the view drawn in Figure 2. The proposed approach consists in establishing Modulation Transfer Functions relating the variance of the SWH to the resulting variance of estimated SSH and SWH. The variations of SWH are then related to the surface envelope, whose bidirectional spectrum is estimated numerically for a gaussian swell spectrum. The products of this spectrum with the MTFs are integrated in azimuth, leading to the desired spectra, which are compared to those obtained from simulated altimetric data. Finally, the semi-analytic model is used to perform regressions over a large number of swell parameters, providing simple expressions for the magnitude and cutoff frequencies of the spectra of estimated SWH and SSH.

2. *Derivation of the modulation transfer functions*

The full altimetric profile is considered as the result of integrating the gaussian surface elevation distribution successively over the y and x directions:

$$AP(z) \propto \frac{1}{\sqrt{2\pi}\sigma_z(x)} \iint_{-\infty}^{+\infty} exp\left\{-\left(\frac{z-\frac{x^2+y^2}{2Z_{sat}}}{\sqrt{2}\sigma_z(x)}\right)^2\right\} dy\, dx$$

(1)

It can be viewed as an average of local profiles $AP(z,x)$ distributed along x, with

$$AP(z,x) \equiv \frac{1}{\sqrt{2\pi}\sigma_z(x)} \int_{-\infty}^{+\infty} exp\left\{-\left(\frac{z-\frac{x^2+y^2}{2Z_{sat}}}{\sqrt{2}\sigma_z(x)}\right)^2\right\} dy$$

(2)

There is no analytic expression for this integral, but it is interesting to observe that it can be written:

$$AP(z,x) \equiv \frac{2^{3/4}}{\sqrt{2\pi}} \sqrt{\frac{Z_{sat}}{\sigma_z(x)}} \int_{-\infty}^{+\infty} e^{-\left(\zeta-Y^2\right)^2} dY$$

(3)

With:

$$Y \equiv \frac{y}{2^{3/4}\sqrt{Z_{sat}\sigma_z(x)}}$$

And

$$\zeta \equiv \frac{z-\frac{x^2}{2Z_{sat}}}{\sqrt{2}\sigma_z(x)}$$

(4)

Thus

$$AP(z,x) = \frac{2^{\frac{3}{4}}}{\sqrt{2\pi}} \sqrt{\frac{Z_{sat}}{\sigma_z(x)}}\, AP_0(\zeta)$$

(5)

Where

$$AP_0(\zeta) \equiv \int_{-\infty}^{+\infty} e^{-\left(\zeta-y^2\right)^2} dy$$

(6)

The final altimetric profile the reads:

$$AP(z) \propto \frac{2^{\frac{3}{4}}}{\sqrt{2\pi}}\sqrt{Z_{sat}}\int_{-\infty}^{+\infty}\frac{AP_0(\zeta(x))}{\sqrt{\sigma_z(x)}}dx$$

(7)

From those expressions, the function $AP_0(\zeta)$ can be tabulated, and the shape of the altimetric profile $AP(z)$ can be computed, given $\sigma_z(x)$. To numerically estimate the MTF, a harmonic variation is considered:

$$\sigma_z(x) = \overline{\sigma_z} + \Delta\sigma_z \cos\left(k_{\sigma_z}x + \varphi_{\sigma_z}\right)$$

(8)

The epoch z_0 is simply defined as the middle point of the ascending front:

$$AP(\widehat{z_0}) = \frac{1}{2}\max\,[AP(z)]$$

(9)

For each sampled wavenumber k_{σ_z}, $\widehat{z_0}$ is estimated for φ_{σ_z} is sampled in $[0,2\pi]$, providing $\widehat{z_0}\left(k_{\sigma_z}, \varphi_{\sigma_z}\right)$. The amplitude MTF is then computed as

$$A_{\widehat{z_0}}\left(\overline{\sigma_z}, \Delta\sigma_z, k_{\sigma_z}\right) = \frac{1}{\pi\Delta\sigma_z}\int_0^{2\pi} cos\varphi_{\sigma_z}\widehat{z_0}\left(k_{\sigma_z}, \varphi_{\sigma_z}\right)d\varphi_{\sigma_z}$$

(10)

The MTF then reads:

$$MTF_{\widehat{z_0}}\left(\overline{\sigma_z}, \Delta\sigma_z, k_{\sigma_z}\right) = \frac{1}{2}\left|A_{\widehat{z_0}}\left(\overline{\sigma_z}, \Delta\sigma_z, k_{\sigma_z}\right)\right|^2$$

(11)

In case of a strictly linear response, the MTF should depend neither on $\overline{\sigma_z}$ nor on $\Delta\sigma_z$. The second harmonic which can be estimated as

$$A'_{\widehat{z_0}}\left(\overline{\sigma_z}, \Delta\sigma_z, k_{\sigma_z}\right) = \frac{1}{\pi\Delta\sigma_z}\int_0^{2\pi} cos\left(2\varphi_{\sigma_z}\right)\widehat{z_0}\left(k_{\sigma_z}, \varphi_{\sigma_z}\right)d\varphi_{\sigma_z}$$

(12)

would also vanish.

The following plot shows the function $AP_0(\zeta)$ defined through equation (6).

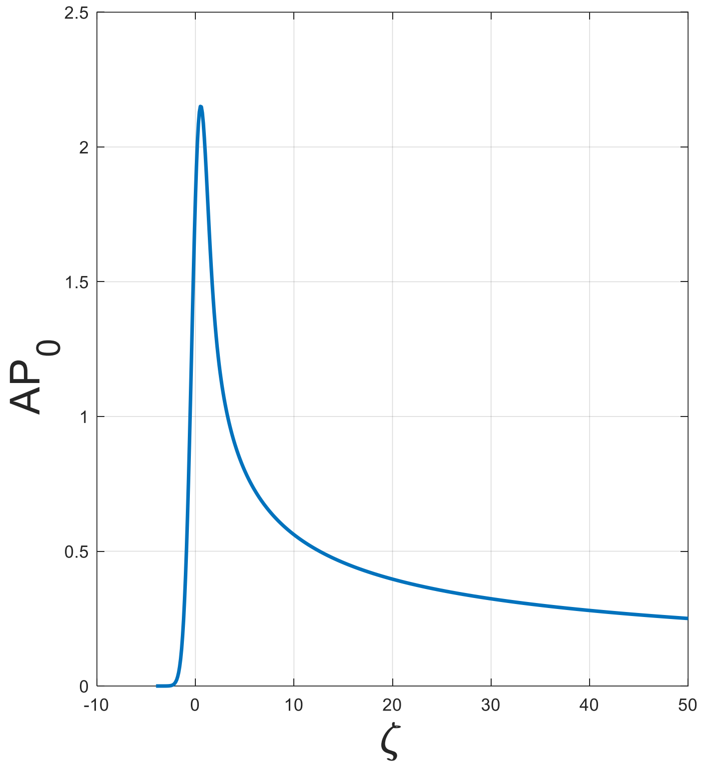

Figure 3 : tabulated function $AP_0(\zeta)$

The following plot shows an altimetric profile computed according eq. (7) for an unperturbed SWH ($\Delta\sigma_z = 0$) (in black), and corresponding profiles for $\frac{\Delta\sigma_z}{\overline{\sigma_z}} = 0.2$, with $\varphi_{\sigma_z} = 0$ and $\varphi_{\sigma_z} = \pi$ (in red and blue). Correspondingly, the midpoint altitude is shifted around 0, with an amplitude of δz_0.

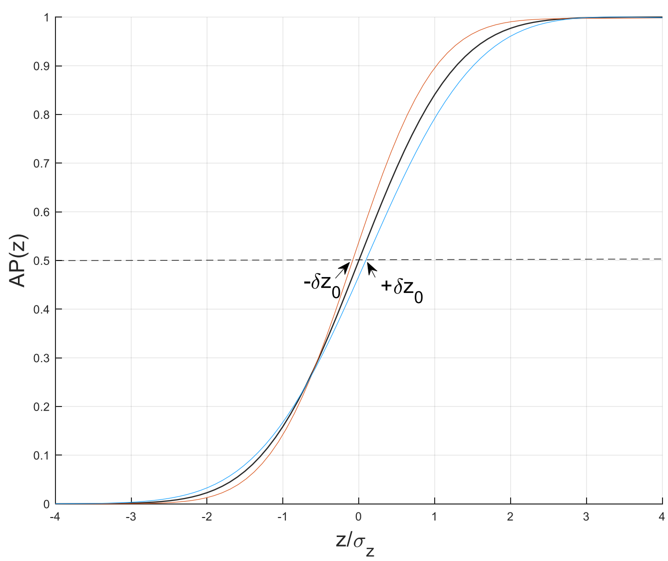

Figure 4 : altimetric profiles AP(z) for unperturbed SWH (black line) and modulated SWH with phase π (in blue) and zero (in red).

On Figure 5 is plotted the displacement of the midpoint $\Delta z_0(k_{\sigma_z}, \varphi_{\sigma_z})/\Delta\sigma_z$ as a function of the modulation wavenumber k_{σ_z}/k_0 and phase φ_{σ_z}. The amplitude is found to exhibit a maximum at a wavenumber close to

$$k_0 \equiv \left(\frac{2}{\pi}\sqrt{\overline{\sigma}_z Z_{sat}}\right)^{-1} \tag{13}$$

From which we can define

$$K \equiv k/k_0 = k\,\frac{2}{\pi}\sqrt{\overline{\sigma}_z Z_{sat}} \tag{14}$$

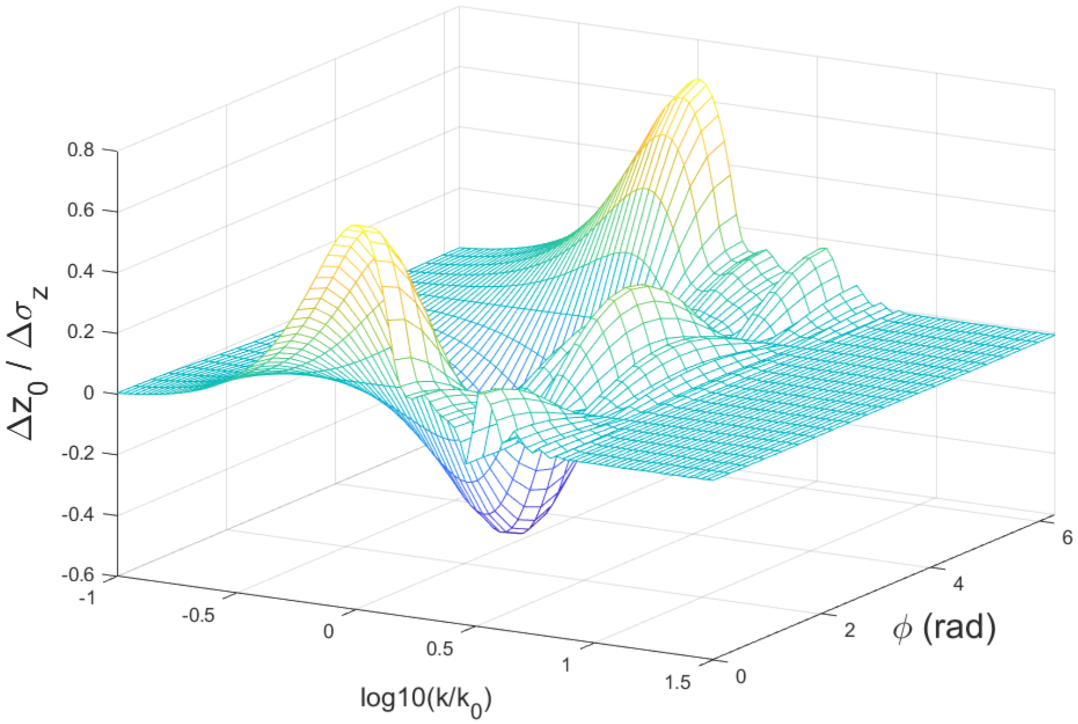

Figure 5 displacement of the midpoint $\Delta z_0(k_{\sigma_z}, \varphi_{\sigma_z})/\Delta\sigma_z$ as a function of the modulation wavenumber k_{σ_z}/k_0 and phase φ_{σ_z}

The observed maximum is in qualitative accordance with the initially anticipated wavelength (eq. (0)). Local maxima are observed at $2k_0$, $3k_0$… The response in phase at k_0 is fairly linear (thus harmonic), while it becomes highly nonlinear at higher frequencies.

The amplitudes $A_{\widehat{z_0}}(\overline{\sigma_z}, \Delta\sigma_z, k_{\sigma_z})$ and $A'_{\widehat{z_0}}(\overline{\sigma_z}, \Delta\sigma_z, k_{\sigma_z})$ obtained by Fourier-analyzing this function (eq. 10-12), with $\overline{\sigma_z} = 0.25\,m$ and $\Delta\sigma_z = 0.01\overline{\sigma_z}$, are plotted on Figure 6. The nonlinearity of the response, roughly given by $|A_2/A_1|$, becomes significant beyond the peak.

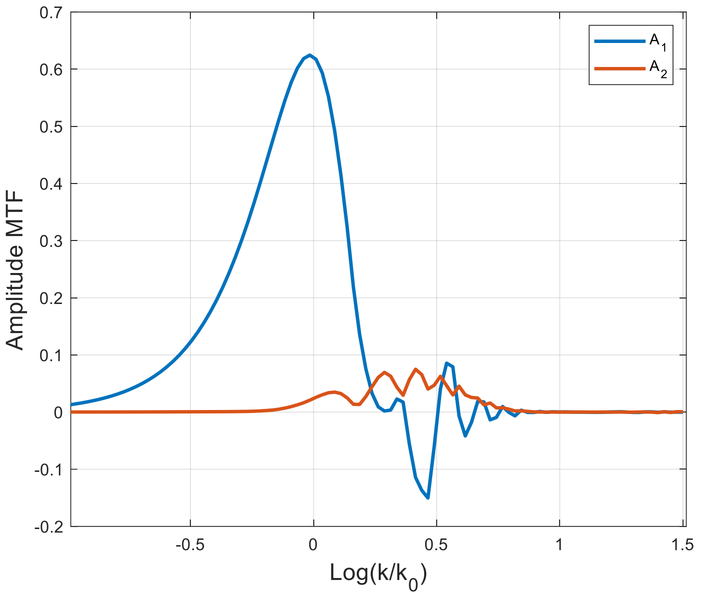

Figure 6 : amplitudes $A_{\widehat{z_0}}\left(\overline{\sigma_z}, \Delta\sigma_z, k_{\sigma_z}\right)$ *and* $A'_{\widehat{z_0}}\left(\overline{\sigma_z}, \Delta\sigma_z, k_{\sigma_z}\right)$*, computed for* $\Delta\sigma_z/\overline{\sigma_z} = 0.01$

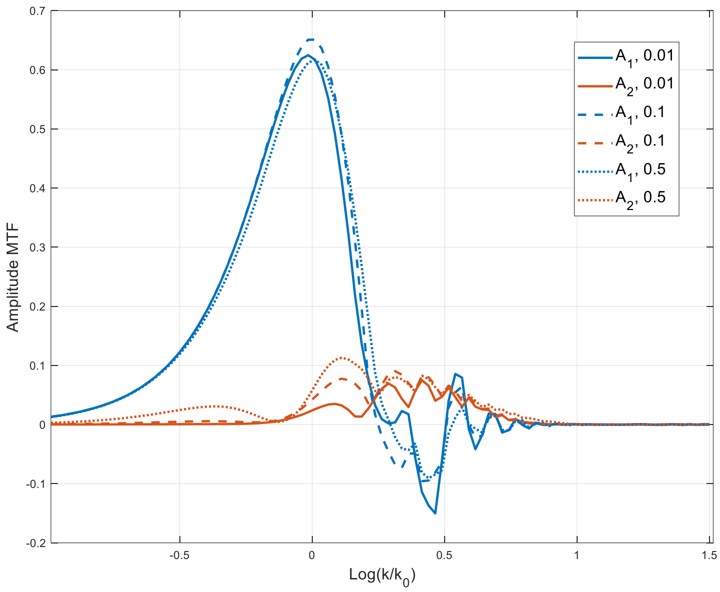

Figure 7 : amplitudes $A_{\widehat{z_0}}\left(\overline{\sigma_z}, \Delta\sigma_z, k_{\sigma_z}\right)$ *and* $A'_{\widehat{z_0}}\left(\overline{\sigma_z}, \Delta\sigma_z, k_{\sigma_z}\right)$*, computed for* $\frac{\Delta\sigma_z}{\overline{\sigma_z}} = 0.01,\ 0.1$ *and* 0.5

Figure 7 presents the same data, plotted for three values of the modulation relative amplitude $\Delta\sigma_z/\overline{\sigma_z} = 0.01,\ 0.1,\ 0.5$, showing that a reasonably linear behaviour may be assumed from low frequencies to the main peak in the vicinity of k_0. From now on, we will adopt the linear response approximation and consider the MTF as defined by eq. (11), and plotted on Figure 8. In this frame, the bidimensional spectra of the epoch $S_{\widehat{z_0}}\left(\boldsymbol{k}_{\sigma_z}\right)$ and the waves enveloppe $S_{\sigma_z}\left(\boldsymbol{k}_{\sigma_z}\right)$ relate through:

$$S_{\widehat{z_0}}(\boldsymbol{k}_{\sigma_z}) = S_{\sigma_z}(\boldsymbol{k}_{\sigma_z})\, MTF_{\widehat{z_0}}(K_{\sigma_z}) = S_{\sigma_z}(\boldsymbol{k}_{\sigma_z})\, MTF_{\widehat{z_0}}(\|\boldsymbol{k}_{\sigma_z}\|/k_0)$$

(15)

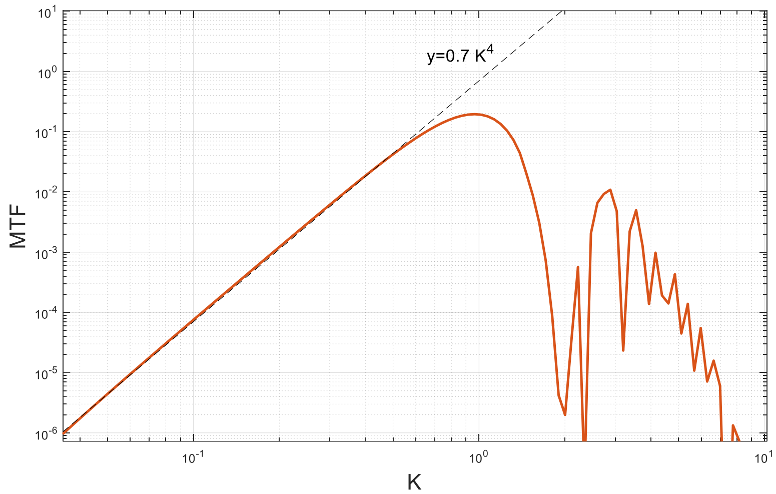

Figure 8 $MTF_{\widehat{z_0}}(K)$ and low frequency approximation

As long as we refer to wave vectors, the power transfer function from σ_z to z_0 doesn't depend on the azimuth direction of the modulation (no selectivity in azimuth). However, when accounting for the satellite motion, modulation wavenumber k_{σ_z} is converted into time frequency, which can be in turn interpreted as an apparent wavenumber k'_{σ_z} :

$$k'_{\sigma_z} \equiv k_{\sigma_z} cos(\Phi_{\sigma_z}) = \frac{K_{\sigma_z}}{x_{max}} cos(\Phi_{\sigma_z})$$

(27)

Where Φ_{σ_z} is the azimuth angle of the harmonic modulation of σ_z with respect to the satellite velocity vector. The power density at $(k_{\sigma_z}, \Phi_{\sigma_z})$ will thus contribute to the measured power density at $k'_{\sigma_z} = k_{\sigma_z} cos(\Phi_{\sigma_z})$. The 1D PSD in k'_{σ_z} results from an integration over the azimuth of the 2D PSD in $\boldsymbol{k}_{\sigma_z}$:

$$S_{\widehat{z_0}}(k'_{\sigma_z}) dk'_{\sigma_z} = \int_{-\frac{\pi}{2}}^{\frac{\pi}{2}} S_{\widehat{z_0}}(\boldsymbol{k}_{\sigma_z}) k_{\sigma_z} dk_{\sigma_z} d\Phi_{\sigma_z}$$

(28)

Given the relation between k'_{σ_z} and k_{σ_z}:

$$S_{\widehat{z_0}}(k'_{\sigma_z}) = \int_{-\frac{\pi}{2}}^{\frac{\pi}{2}} \frac{1}{cos^2\Phi_{\sigma_z}} S_{\widehat{z_0}}\left(\frac{k'_{\sigma_z}}{cos\Phi_{\sigma_z}}, \Phi_{\sigma_z}\right) k'_{\sigma_z} d\Phi_{\sigma_z}$$

(29)

Or, introducing $S_{\sigma_z}(\boldsymbol{k}_{\sigma_z})$,

$$S_{\widehat{z_0}}(k'_{\sigma_z}) = k'_{\sigma_z}\int_{-\frac{\pi}{2}}^{\frac{\pi}{2}} \frac{1}{cos^2\Phi_{\sigma_z}} S_{\sigma_z}\left(\frac{k'_{\sigma_z}}{cos\Phi_{\sigma_z}}, \Phi_{\sigma_z}\right) MTF_{\widehat{z_0}}\left(\frac{k'_{\sigma_z}}{k_0 cos\Phi_{\sigma_z}}\right) d\Phi_{\sigma_z}$$

(30)

This expression allows estimating numerically the epoch spectrum from the MTF, if we have a knowledge of the bidimensional envelope spectrum.

Figure 9 provides a visual interpretation of eq. (30). It shows the circularly-symmetric $MTF_{\widehat{z_0}}$ in the bidimensional (k_x, k_y) space. From eq. (30), $S_{\widehat{z_0}}(k'_{\sigma_z})$ is obtained by integrating the product $S_{\sigma_z} MTF_{\widehat{z_0}}$ along k_y (red curves). Considering S_{σ_z} as constant for simplicity, the integral is performed on slices of $MTF_{\widehat{z_0}}$, the shape of the integrand can be assimilated to that of the MTF slice. This explains the low-frequency plateau, the weak maximum and the subsequent fall-off.

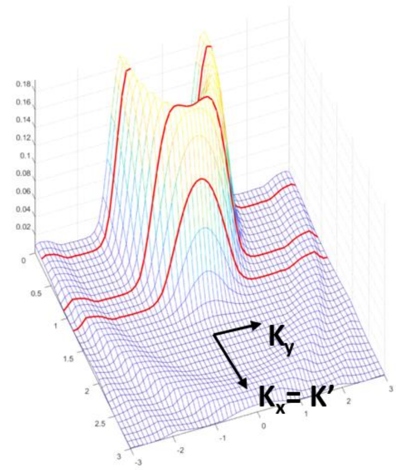

Figure 9 : circularly-symmetric $MTF_{\widehat{z_0}}$ in the bidimensional (k_x, k_y) space

Before going into numerical study, it is instructive to illustrate the overall behaviour of $S_{z_0}(k'_{\sigma_z})$ by considering a very crude approximation to he FTM, illustrated on Figure 8:

$$MTF_{\widehat{z_0}}(K) \sim aK^4 \qquad \text{for } K < 1$$

(31)

We consider a constant envelope spectrum over the wavenumber domain in which the FTM is non-zero:

$$S_{\sigma_z}(k_{\sigma_z}, \Phi_{\sigma_z}) \equiv S_{\sigma_z}$$

(32)

Eq. (30) thus becomes:

$$S_{\widehat{z_0}}(k'_{\sigma_z}) = 2aS_{\sigma_z}\frac{{k'_{\sigma_z}}^5}{k_0^4}\int_0^{acos\left(\frac{k'_{\sigma_z}}{k_0}\right)} cos^{-6}\Phi_{\sigma_z} d\Phi_{\sigma_z}$$

(33)

$cos^{-6}\Phi_{\sigma_z}$ can be integrated analytically, leading to:

$$S_{\widehat{z_0}}(k'_{\sigma_z}) = 2aS_{\sigma_z}k_0\,\frac{1}{15}(3+4K^2+8K^4)\sqrt{1-K^2}$$
$$= \frac{\pi}{5}\,\frac{aS_{\sigma_z}}{\sqrt{\overline{\sigma_z}Z_{sat}}}\left(1+\frac{4}{3}K^2+\frac{8}{3}K^4\right)\sqrt{1-K^2}$$

(34)

With $K \equiv k'_{\sigma_z}/k_0$

The function setting the spectral dependance in K is plotted on Figure 10, showing how integrating over the azimuth shifts and smears the MTF peak. The main point is that this spectral shape is essentially a plateau from low frequencies to $0.82k_0$, varying only from 1 to 1.78 on this frequency range.

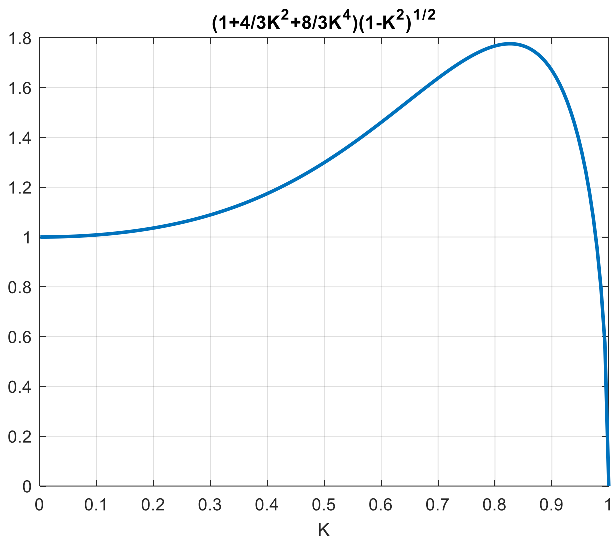

Figure 10: shape of the K dependency in eq. (34)

The zero-frequency limit, which also gives the overall level of the spectrum, simply reads:

$$S_{\widehat{z_0}}(k'_{\sigma_z} \to 0) = \frac{\pi}{5}\,\frac{aS_{\sigma_z}}{\sqrt{\overline{\sigma_z}Z_{sat}}}$$

Comparison with numerical integration with the exact MTF suggests $a = 2/3$:

$$S_{\widehat{z_0}}(k'_{\sigma_z} \to 0) = \frac{2\pi}{15}\,\frac{S_{\sigma_z}}{\sqrt{\overline{\sigma_z}Z_{sat}}}$$

(35)

So that a better approximate tot the PSD at low frequency is:

$$S_{\widehat{Z_0}}(k'_{\sigma_z}) \approx \frac{2\pi}{15} \frac{S_{\sigma_z}}{\sqrt{\overline{\sigma_z} Z_{sat}}} \left(1 + \frac{4}{3}K^2 + \frac{8}{3}K^4\right)\sqrt{1 - K^2}$$

(36)

Figure 11 show how it compares with the numerical integration of eq. (30), when taking $S_{\sigma_z} = 1$, for $\overline{\sigma_z} = 0.25\ m$ and $2.5\ m$. The zero-frequency asymptote closely follows eq. (36), while the peak at $\sim 0.8\ k_0$ is even smaller, at about 1.4 times the zero-frequency limit. This spectral shape describes a plateau much more than a bump.

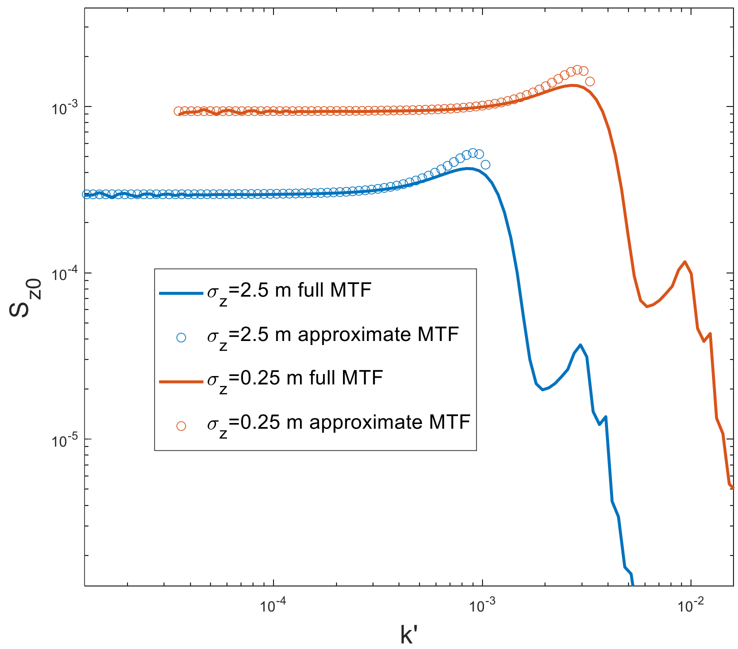

Figure 11: shape of $S_{\widehat{Z_0}}(k'_{\sigma_z})$ in case of unit modulating spectrum $S_{\sigma_z} = 1$ for two values of the surface elevation std and corresponding approximation from eq. (34)

All this development may be repeated for the estimated height standard deviation $\widehat{\sigma_z}$, the corresponding MTF being defined through:

$$A_{\widehat{\sigma_z}}(\overline{\sigma_z}, \Delta\sigma_z, k_{\sigma_z}) = \frac{1}{\pi\Delta\sigma_z}\int_0^{2\pi} cos\varphi_{\sigma_z}\widehat{\sigma_z}(k_{\sigma_z}, \varphi_{\sigma_z})d\varphi_{\sigma_z}$$

$$MTF_{\widehat{\sigma_z}}(\overline{\sigma_z}, \Delta\sigma_z, k_{\sigma_z}) = \frac{1}{2}\left|A_{\widehat{\sigma_z}}(\overline{\sigma_z}, \Delta\sigma_z, k_{\sigma_z})\right|^2$$

(37)

To numerically compute $MTF_{\widehat{\sigma_z}}$, we estimate the fluctuations of $\widehat{\sigma_z}$ from the gradient of the altimetric profile at its midpoint:

$$\widehat{\sigma_z} \equiv \overline{\sigma_z} \frac{\langle \partial_z AP \rangle}{\partial_z AP}\bigg|_{\widehat{z_0}}$$

(38)

Where $\partial_z AP$ is the profile gradient and $\langle \partial_z AP \rangle$ its average over φ_{σ_z}.

The numerically estimated amplitudes $A_{\widehat{\sigma_z}}$ and $A'_{\widehat{\sigma_z}}$ are plotted on Figure 12. As expected, $A_{\widehat{\sigma_z}}$ is close to unity as long as the frequency is much smaller than k_0. It then exhibits only a very weak bump before a steep fall around k_0, followed by damped oscillations.

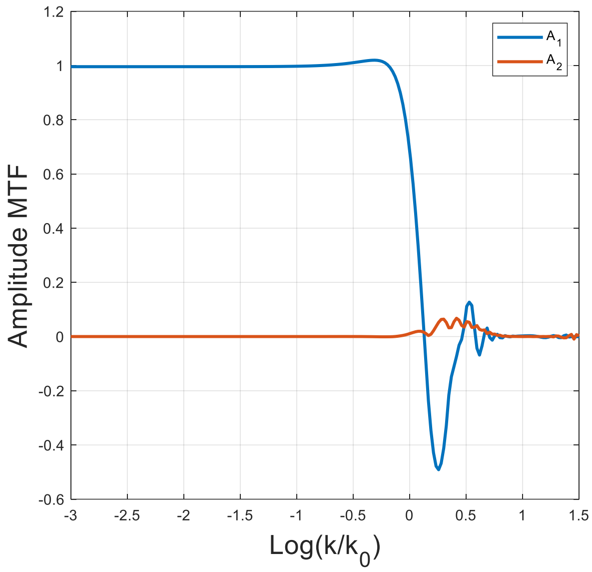

Figure 12: amplitude MTF $MTF_{\widehat{\sigma_z}}(K)$ for the measured surface elevation std $\widehat{\sigma_z}$

As previously, the along-track $\widehat{\sigma_z}$ spectrum $S_{\widehat{\sigma_z}}(k'_{\sigma_z})$ is obtain by integrating on the modulation azimuth:

$$S_{\widehat{\sigma_z}}(k'_{\sigma_z}) = k'_{\sigma_z} \int_{-\frac{\pi}{2}}^{\frac{\pi}{2}} \frac{1}{cos^2\Phi_{\sigma_z}} S_{\sigma_z}\left(\frac{k'_{\sigma_z}}{cos\Phi_{\sigma_z}}, \Phi_{\sigma_z}\right) MTF_{\widehat{\sigma_z}}\left(\frac{k'_{\sigma_z}}{k_0 cos\Phi_{\sigma_z}}\right) d\Phi_{\sigma_z}$$

(39)

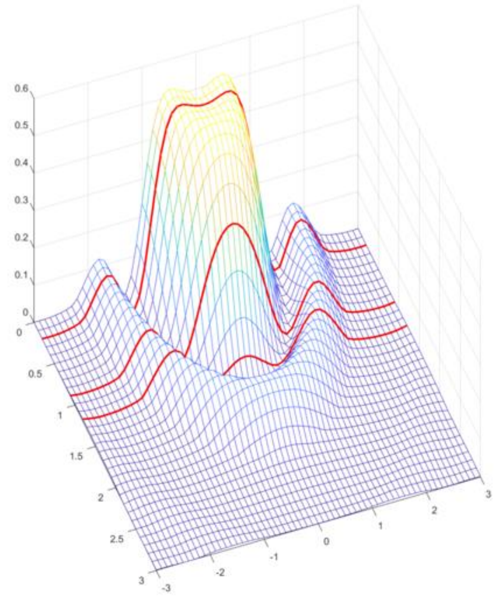

Figure 13 : circularly-symmetric $MTF_{\widehat{\sigma_z}}$ in the bidimensional (k_x, k_y) space

Under the following approximation:

$$MTF_{\widehat{\sigma_z}}(K) \equiv 1\,, K < 1$$
$$MTF_{\widehat{\sigma_z}}(K) \equiv 0\,, K \geq 1$$

(40)

Eq. (39) gives:

$$S_{\widehat{\sigma_z}}\left(k'_{\sigma_z}\right) \approx 2S_{\sigma_z}k_0\sqrt{1-K^2}$$
$$= \frac{\pi S_{\sigma_z}}{\sqrt{\overline{\sigma_z}Z_{sat}}}\sqrt{1-K^2}$$

(41)

As previously, a better simplified expression is obtained through numerical integration:

$$S_{\widehat{\sigma_z}}\left(k'_{\sigma_z}\right) \approx \frac{4\pi}{7}\frac{S_{\sigma_z}}{\sqrt{\overline{\sigma_z}Z_{sat}}}\sqrt{1-K^2}$$

(42)

Even in this simplified form, $S_{\widehat{\sigma_z}}\left(k'_{\sigma_z}\right)$ presents no bump, contrary to $S_{\widehat{Z_0}}\left(k'_{\sigma_z}\right)$ (eq. (36)). Moreover, at low frequency:

$$\frac{S_{\widehat{\sigma_z}}}{S_{\widehat{Z_0}}}\left(k'_{\sigma_z} \to 0\right) \approx \frac{30}{7}$$

On Figure 14 are plotted $S_{\widehat{\sigma_z}}(k'_{\sigma_z})$ and $S_{\widehat{z_0}}(k'_{\sigma_z})$ with corresponding approximations (from eq. (36) and (41)), for $S_{\sigma_z} = 1$, $\overline{\sigma_z} = 1.25m$, $Z_{sat} = 800\ km$.

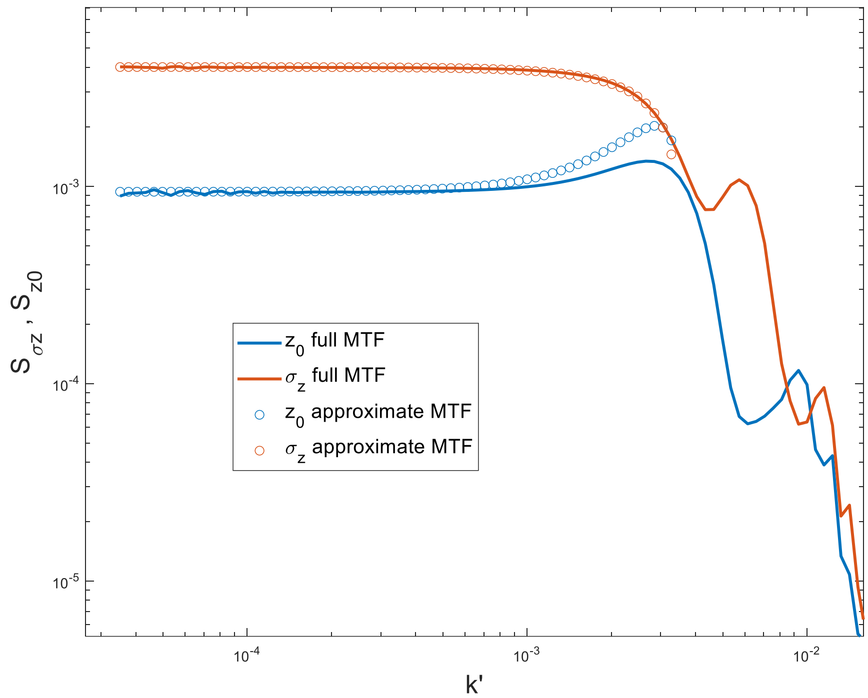

Figure 14: shape of $S_{\widehat{\sigma_z}}(k'_{\sigma_z})$ and $S_{\widehat{z_0}}(k'_{\sigma_z})$ and in case of unit modulating spectrum $S_{\sigma_z} = 1$ and corresponding approximation from eq. (42)

3. SWH-SSH cross spectrum and coherence

In the previous, considered variations of estimated SHH entirely result from SWH variations. In real data, however, this effect superimposes over other variations patterns, which are not - or not directly - related to SWH. The cross spectrum of estimated SWH and SSH could thus help identifying the part of SSH fluctuations that may be related to SWH ones, in order to validate the present work, and to reduce the contribution of SWH in SSH spectra.

The cross spectrum $S_{\widehat{z_0}\widehat{\sigma_z}}(k'_{\sigma_z})$ may be derived from re-writing eq. (29) in terms of complex amplitudes:

$$A_{\widehat{z_0}}(k'_{\sigma_z}) = \sqrt{k'_{\sigma_z}} \int_{-\frac{\pi}{2}}^{\frac{\pi}{2}} \frac{1}{cos\Phi_{\sigma_z}} S_{\sigma_z}^{1/2}(\Phi_{\sigma_z}) \mathcal{N}(\Phi_{\sigma_z}) A_{\widehat{z_0}}(\Phi_{\sigma_z}) d\Phi_{\sigma_z}$$

(43)

Where the dependencies in k'_{σ_z} have been dropped in the integrand for simplicity. $\mathcal{N}(\Phi_{\sigma_z})$ is a circularly-symmetric complex normal distribution. As the corresponding expression can also be written for $A_{\widehat{\sigma_z}}(k'_{\sigma_z})$, the cross-spectrum reads:

$$S_{\widehat{z_0}\widehat{\sigma_z}}(k'_{\sigma_z}) = \frac{1}{2} \langle A_{\widehat{z_0}}(k'_{\sigma_z})\ A^*_{\widehat{\sigma_z}}(k'_{\sigma_z}) \rangle$$

$$= \frac{1}{2}\langle k'_{\sigma_z} \iint \frac{1}{cos\Phi_{\widehat{z_0}} cos\Phi_{\widehat{\sigma_z}}} \mathcal{N}(\Phi_{\widehat{z_0}})\mathcal{N}^*(\Phi_{\widehat{\sigma_z}}) S_{\sigma_z}^{\frac{1}{2}}(\Phi_{\widehat{z_0}}) S_{\sigma_z}^{\frac{1}{2}}(\Phi_{\widehat{\sigma_z}}) A_{\widehat{z_0}}(\Phi_{\widehat{z_0}}) A_{\widehat{\sigma_z}}(\Phi_{\widehat{\sigma_z}}) d\Phi_{\widehat{z_0}} d\Phi_{\sigma_z}\rangle$$

$$= \frac{1}{2} k'_{\sigma_z} \iint \frac{1}{cos\Phi_{\widehat{z_0}} cos\Phi_{\widehat{\sigma_z}}} \langle\mathcal{N}(\Phi_{\widehat{z_0}})\mathcal{N}^*(\Phi_{\widehat{\sigma_z}})\rangle S_{\sigma_z}^{\frac{1}{2}}(\Phi_{\widehat{z_0}}) S_{\sigma_z}^{\frac{1}{2}}(\Phi_{\widehat{\sigma_z}}) A_{\widehat{z_0}}(\Phi_{\widehat{z_0}}) A_{\widehat{\sigma_z}}(\Phi_{\widehat{\sigma_z}}) d\Phi_{\widehat{z_0}} d\Phi_{\sigma_z}$$

Assuming that $\langle\mathcal{N}(\Phi_{\widehat{z_0}})\mathcal{N}(\Phi_{\widehat{\sigma_z}})\rangle = \delta_{\Phi_{\widehat{z_0}},\Phi_{\widehat{\sigma_z}}}$, the cross-spectrum finally writes, consistently with the self-spectra:

$$S_{\widehat{z_0}\widehat{\sigma_z}}(k'_{\sigma_z}) = \frac{1}{2} k'_{\sigma_z} \int_{-\frac{\pi}{2}}^{\frac{\pi}{2}} \frac{1}{cos^2\Phi_{\sigma_z}} S_{\sigma_z}\left(\frac{k'_{\sigma_z}}{cos\Phi_{\sigma_z}}, \Phi_{\sigma_z}\right) A_{\widehat{z_0}} A_{\widehat{\sigma_z}}\left(\frac{k'_{\sigma_z}}{k_0 cos\Phi_{\sigma_z}}\right) d\Phi_{\sigma_z} \tag{44}$$

Following approximations given by eq. (31) and (40),

$$\frac{1}{2} A_{\widehat{z_0}} A_{\widehat{\sigma_z}} \sim \sqrt{a} K^2, \quad K < 1 \tag{45}$$

Which leads to

$$S_{\widehat{z_0}\widehat{\sigma_z}}(k'_{\sigma_z}) = 2a^{1/2} S_{\sigma_z} \frac{{k'_{\sigma_z}}^3}{k_0^2} \int_0^{acos\left(\frac{k'_{\sigma_z}}{k_0}\right)} cos^{-4}\Phi_{\sigma_z} d\Phi_{\sigma_z}$$

And

$$S_{\widehat{z_0}\widehat{\sigma_z}}(k'_{\sigma_z}) = \frac{2}{3} a^{\frac{1}{2}} S_{\sigma_z} k_0 (2K^2 + 1)\sqrt{1 - K^2} \tag{46}$$

Even more interesting than the cross-spectrum is the magnitude-squared coherence (called simply "coherence" hereafter):

$$C_{\widehat{z_0}\widehat{\sigma_z}}(k'_{\sigma_z}) \equiv \frac{\left|S_{\widehat{z_0}\widehat{\sigma_z}}(k'_{\sigma_z})\right|^2}{S_{\widehat{z_0}} S_{\widehat{\sigma_z}}}$$

$$C_{\widehat{z_0}\widehat{\sigma_z}}(k'_{\sigma_z}) = \frac{\left(\int_{-\frac{\pi}{2}}^{\frac{\pi}{2}} S_{\sigma_z} cos^{-2}\Phi_{\sigma_z} A_{\widehat{z_0}} A_{\widehat{\sigma_z}} d\Phi_{\sigma_z}\right)^2}{\left(\int_{-\frac{\pi}{2}}^{\frac{\pi}{2}} S_{\sigma_z} cos^{-2}\Phi_{\sigma_z} A_{\widehat{z_0}}^2 d\Phi_{\sigma_z}\right)\left(\int_{-\frac{\pi}{2}}^{\frac{\pi}{2}} S_{\sigma_z} cos^{-2}\Phi_{\sigma_z} A_{\widehat{\sigma_z}}^2 d\Phi_{\sigma_z}\right)} \tag{47}$$

This latter expression (in which dependencies in in k'_{σ_z} and Φ_{σ_z} are omitted) accounts for the fact that, in the present case, $A_{\widehat{z_0}}$ and $A_{\widehat{\sigma_z}}$ are real-valued. It shows that, were $A_{\widehat{z_0}}/A_{\widehat{\sigma_z}}$ independent of the frequency, then coherence would equal unity. But, as we previously saw, $A_{\widehat{z_0}}$ and $A_{\widehat{\sigma_z}}$ have different frequency behaviors, hence $C_{\widehat{z_0}\widehat{\sigma_z}}(k'_{\sigma_z}) < 1$, even with no external contributions (other sources of fluctuations or noise).

Using the previously derived approximations (eq. (34), (41) and (46)), the behaviour of $C_{\widehat{z_0}\widehat{\sigma_z}}(k'_{\sigma_z})$ for $k'_{\sigma_z} < k_0$ qualitatively follows that of:

$$C_{\widehat{z_0}\widehat{\sigma_z}}\left(K = \frac{k'_{\sigma_z}}{k_0}\right) \sim \frac{15}{9}\frac{(2K^2+1)^2}{3+4K^2+8K^4} \tag{48}$$

According this simple expression, the coherence reaches a maximum at $C_{\widehat{z_0}\widehat{\sigma_z}}(K'=1) = 1$. This results from the approximation we made that if $K' > 1,\ A_{\widehat{z_0}} = 0$ and $A_{\widehat{\sigma_z}} = 0$. It follows that if $K' = 1, A_{\widehat{z_0}}\left(K'/cos\Phi_{\sigma_z}\right) = \ \delta_{\Phi_{\sigma_z}} A_{\widehat{z_0}}(K' = 1)$. Integrals in (47) then reduce to sampling at $K' = 1$, leading to $C_{\widehat{z_0}\widehat{\sigma_z}}(K'=1) = 1$. At low frequency, $C_{\widehat{z_0}\widehat{\sigma_z}}(K'=0) = \frac{5}{9} = 0.56$. The figure bellow

Shows the approximation given by eq. (48) and the coherence curves obtained by numerical computation of eq. (47) ("full MTF") and from simulated altimetric data (for sea state 1, see hereafter).

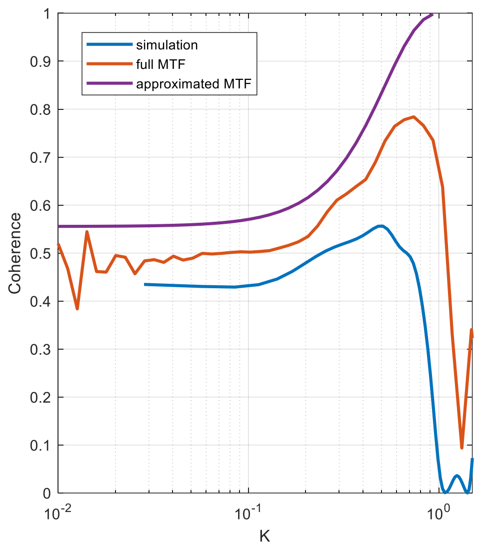

Figure 15

Similar shapes are obtained, even if the maxima exact location and magnitude vary.

Figure 16 shows both MTFs to help understand the overall spectral shape of the coherence, which is tightly related to the correlation between the MTF cuts along k_y via the integral $\left(\int_{-\frac{\pi}{2}}^{\frac{\pi}{2}} S_{\sigma_z} cos^{-2}\Phi_{\sigma_z} A_{\widehat{z_0}} A_{\widehat{\sigma_z}} d\Phi_{\sigma_z}\right)^2$. In the vicinity of the bump ($K_x \gtrsim 1$), both MTFs slices present a main lobe centered on $k_y = 0$, hence a significant correlation. At lower frequencies, $MTF_{\widehat{\sigma_z}}$ has the shape of a top-hat centered at $k_y = 0$ while $MTF_{\widehat{z_0}}$ exhibit two symmetric peaks. They are thus very different, leading to lower correlation.

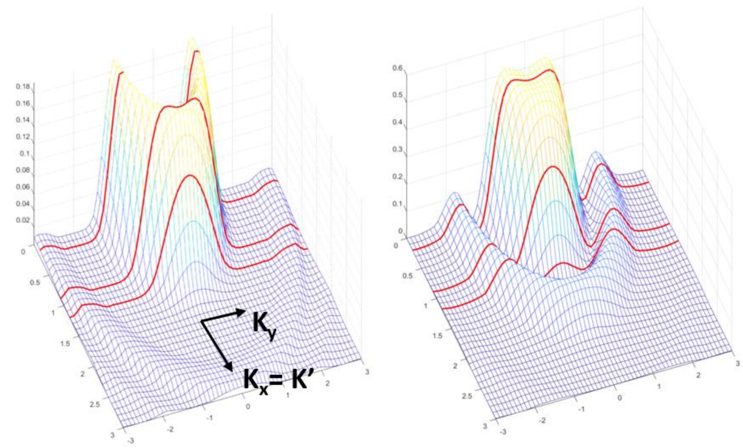

$MTF_{\widehat{z_0}}(K)$ $MTF_{\widehat{\sigma_z}}(K)$

Figure 16 : comparing the MTFs in the bidirectional space helps understanding the overall shape of the coherence spectrum.

4. *Wave groups and the envelope spectrum*

Up to now, we have been concentrating on the power transfer function between possible SWH modulation and subsequent modulation of the measured epoch and SWH. The origin of the modulation, and thus the value of S_{σ_z}, has been left apart.

Wave groups are a good candidate, for they are widespread and cover a wide spatial frequency range, from $k_{\sigma_z} = 0$ to $\sim FWHM_{k_w}$, where $FWHM_{k_w}$is a measurement of the width of the swell spectrum. In most conditions, $FWHM_{k_w}$ should be larger the frequency cut in the power transfer function studied previously, so that the bump fall would be essentially given by K_m/x_{max}, which is only moderately sensitive to the SWH. Furthermore, the "wave group spectrum" is fairly isotropic in azimuth, whatever the dominant direction of the swell. The shape of the bump can thus be expected to be essentially insensitive to the swell direction. For those reasons, wave groups could explain why the spectral bump is so widely present in altimetric data.

The bidirectional spectrum of the standard deviation $S_{\sigma_z}(\boldsymbol{k_{\sigma_z}})$ is considered as proportionnal to he surface envelope spectrum, wihch has been estimated numerically, from realisations oft he surface.

The elevation std spectrum $S_{\sigma_z}(\boldsymbol{k_{\sigma_z}})$ is estimated numerically, for a given sea state defined through:

- A gaussian swell spectrum with given σ_{k_x} and σ_{k_y} standard deviations and a significant wave hight SWH_{swell}
- A wind-sea Elfouhaily spectrum with given U_{10}

From the resulting elevation spectrum, a number of realizations of the surface are generated (through inverse 2D Fourier transform) and their envelopes are derived. The bidirectional envelope spectrum is then estimated (through 2D Fourier transform and averaging over the realizations). The size and resolution of the computed surfaces are chosen to make the low-frequency asymptote accessible.

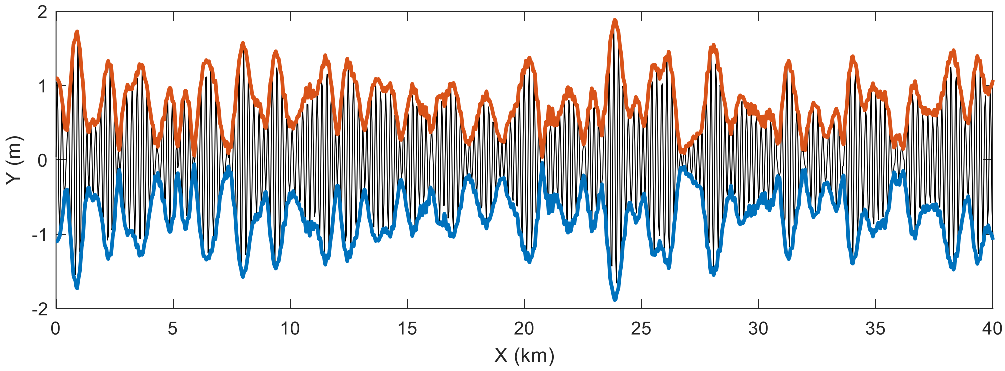

Figure 17: typical cut in the surface elevation map, with upper and lower envelopes.

The envelope $Env(x,y)$ is computed as half the difference between the upper and lower envelopes, as plotted on Figure 17. It is assumed that the envelope is proportional to some "local" surface height standard deviation $\sigma_z(x,y)$ defined as:

$$\sigma_z(x,y) \equiv Env(x,y)\ \frac{\sigma_z}{\langle Env(x,y)\rangle} \tag{49}$$

For the investigated gaussian spectra, $\frac{\sigma_z}{\langle Env(x,y)\rangle} \simeq 0.4$.

For the following experiment, two sea states are considered, with the following swell parameters:

Sea state S1: $SWH_{swell} = 2.5\ m,\ \sigma_{k_x} = \sigma_{k_y} = 0.006\ m^{-1}$

Sea state S2: $SWH_{swell} = 5\ m,\ \sigma_{k_x} = \sigma_{k_y} = 0.003\ m^{-1}$

In both cases, the swell central wavelength is 200 m, and $U_{10} = 7\ m/s$.

On Figure 18 are plotted the corresponding azimuth-averaged bidirectional spectra $S_{\sigma_z}(\boldsymbol{k}_{\sigma_z})$.

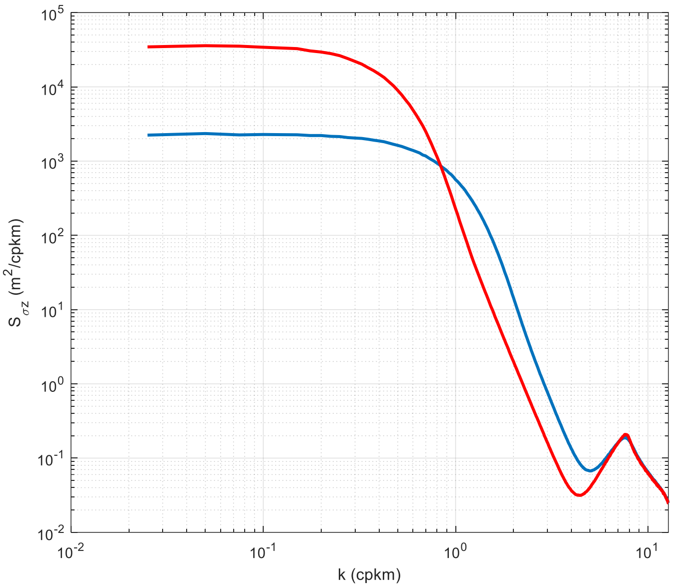

Figure 18 : circularly averaged surface height std bidirectionnal spectrum $S_{\sigma_z}(\boldsymbol{k}_{\sigma_z})$ for two sea states S1 (in blue) and S2 (in red).

The bump around 8 cpkm appears to be related to the wind sea, whose shorter waves are not correctly sampled in this spectrum estimate. To check and more precisely catch this behaviour, the spectrum is estimated at higher resolution, as plotted on Figure 19. While the spectrum for the wind sea alone (in dashed blue) has a gaussian-like shape, a marked bump is confirmed for the swell+wind sea state, even if it remains more than 4 orders of magnitude lower than the zero-frequency level. Due to this very low level and its frequency position far beyond the FTM cutoff, this wind-sea peak need not be accounted for.

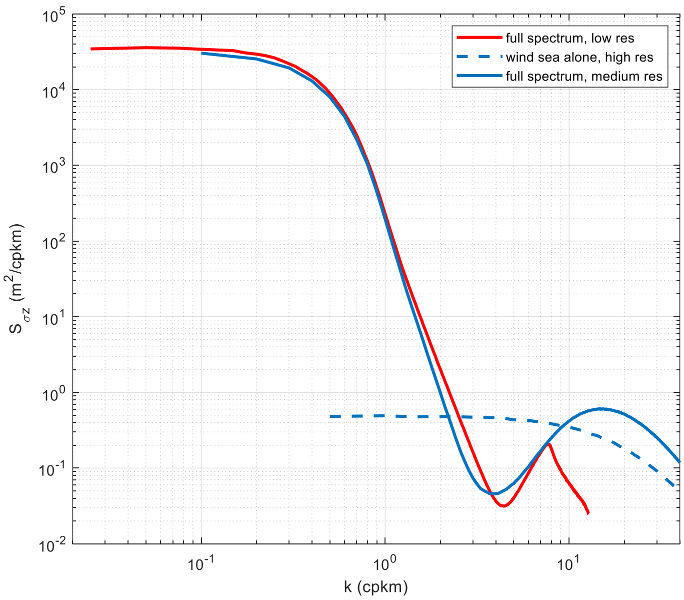

Figure 19 : $S_{\sigma_z}(\boldsymbol{k}_{\sigma_z})$ estimated for with various resolutions and sea states (see text)

The numerically obtained bidirectionnal spectra $S_{\sigma_z}(\boldsymbol{k}_{\sigma_z})$ are used to estimate $S_{\widehat{z_0}}(k'_{\sigma_z})$ and $S_{\widehat{\sigma_z}}(k'_{\sigma_z})$ through numerical integration of eq. (30) and eq. (39) for sea states S1 and S2.

The resulting spectra, based on the previously presented model, are plotted on Figure 20. Also plotted are corresponding spectra obtained through numerical simulation of the Sentinel 3 SRAL altimeter, with the same sea states S1 and S2.

The SRAL simulator essentially reproduces the altimetric measurement process : a gaussian facetted sea surface following the prescribed sea state is generated in the instrument footprint (at 2.5 m resolution). For each emitted pulse, the backscattered wave contribution is computed at the facet level, then integrated in resolution cells, providing the simulated altimetric waveforms. The epoch and SWH are estimated from waveforms generated along 100 km tracks. Corresponding spectra are then estimated by averaging 100 periodograms computed from 100 tracks.

As this simulator was developed to provide realistic synthetic IQ signals, the speckle noise is inherently present as the result of adding numerous complex contributors. However, for the purpose of the present study, it is preferable to get rid of the speckle noise, which can be done simply by summing the average power backscattered from the facets rather than the complex amplitudes. In this way, not only the altimetric profiles, the estimated epoch and SWH and the resulting periodograms are free from speckle noise and its effects, but pulse-averaging is not required anymore, making the simulations much faster. However, power spectral density estimator remains inherently noisy, hence the average over 100 tracks.

As illustrated by Figure 20, the spectra obtained from the simulator and subsequent processing (retracking, PSD estimate) are in good agreement with those computed according the model developed above, at least from low frequencies to the cutoff. In particular, the level of the low-frequency plateau, the cutoff frequency and the shape of the spectrum around the cutoff are precisely caught.

The agreement is quantitatively not so good beyond the cutoff, especially concerning the epoch spectrum. But the expected secondary peaks due to the oscillations of the MTF are actually present in the simulated data. The observed discrepancy could originate from stronger non-linearity at high frequencies (as suggested by the higher contribution from the second harmonic), from the fitting process used for the retracking (which differs from the simple epoch and SWH estimators considered in the model), from the σ_0 dependency to viewing angles (considered in the simulator, not in the model), from the antenna pattern (in the simulator, not in the model)… Nevertheless, the very simple model developed here seems to correctly predict de level and shape of the spectrum over the frequency range accessible to the observations in conventional altimetry.

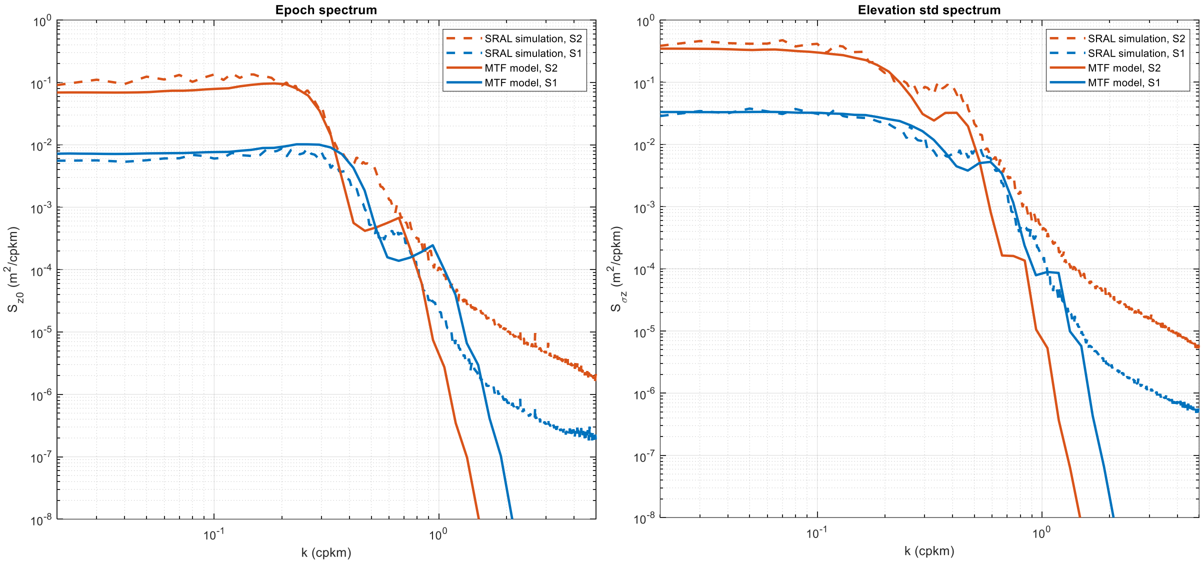

Figure 20 : $S_{\widehat{z_0}}$ (left) and $S_{\widehat{\sigma_z}}$ (right) obtained from synthetic signals from SRAL simulations (dashed lines) and from the present model (solid line) for sea states S1 (blue) and S2 (red)

This is illustrated by Figure 21, where the estimate of $S_{\widehat{z_0}}\left(k'_{\sigma_z}\right)$ obtained from realistic synthetic IQ signals, including speckle noise, is plotted together with the speckle-free version and the model. The speckle noise is reduced through averaging over bursts of 64 pulses. In such conditions, the secondary peaks are not accessible.

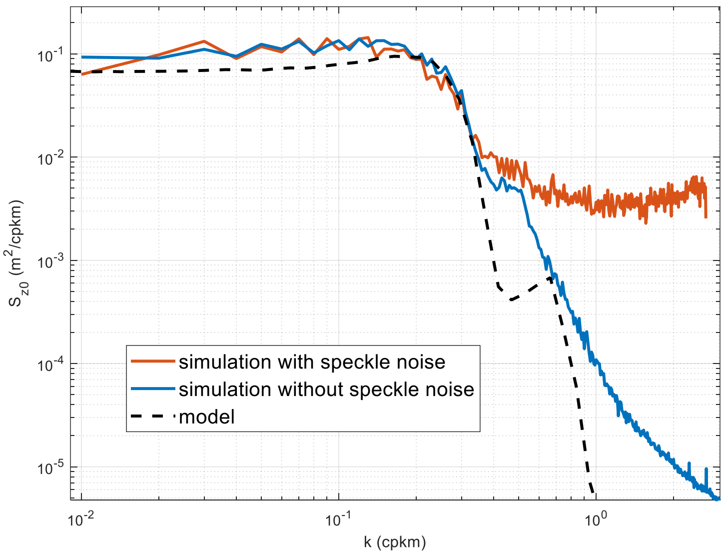

Figure 21 : $S_{\widehat{z_0}}$ (left) in S2 sea state from synthetic signals from SRAL simulations (solid lines) et from the present model (black dashed line). Simulations performed with (in red) and without (in blue) speckle noise.

Although it is based on a very simplified description of the altimetric measurement, the model developed above proves to correctly reproduce the main characteristics of the spectra of the estimated surface elevation and SWH obtained with a realistic simulator. In particular, it provides a correct estimate of the level of the low-frequency plateau (denoted $S^0_{\widehat{z_0}}$ and $S^0_{\widehat{\sigma_z}}$ in the following), and of the corresponding -3 dB cutoff frequency $k^{-3dB}_{\widehat{z_0}}$ and $k^{-3dB}_{\widehat{\sigma_z}}$.

5. Regressions on the low-frequency level and frequency cutoff

Such parameters are also of interest for interpretating real altimetric spectra, especially if they can be related to the sea state. For this purpose, the model is executed for a large number (~6000) of random configurations from which simple empirical laws are then derived. For each configuration, the randomly generated parameters are:

- swell spectrum parameters: SWH_{swell}, mean wave number $\overline{k_{swell}}$ and direction $\overline{\varphi_{swell}}$, gaussian spectrum std in wavenumber σ_{k_x} and azimuth $\sigma_{k_\varphi} = \sigma_{k_y}/\,\overline{k_{swell}}$,
- wind sea: U_{10},
- Satellite altitude Z_{sat}.

The corresponding envelope spectrum $S_{\sigma_z}(\boldsymbol{k}_{\boldsymbol{\sigma}_z})$ is numerically computed according to the previously described procedure. $S_{\widehat{Z_0}}(k'_{\sigma_z})$ and $S_{\widehat{\sigma_z}}(k'_{\sigma_z})$ are then computed (eq. (30) and (39)), from which $S^0_{\widehat{Z_0}}$, $S^0_{\widehat{\sigma_z}}$, $k^{-3dB}_{\widehat{Z_0}}$ and $k^{-3dB}_{\widehat{\sigma_z}}$ are finally estimated.

The swell envelope spectrum $S_{\sigma_z}(\boldsymbol{k}_{\boldsymbol{\sigma}_z})$, and therefore $S^0_{\widehat{Z_0}}$ and $S^0_{\widehat{\sigma_z}}$, can be expected to be approximately proportional to

$$\beta \equiv \frac{\sigma_z^2}{\sigma_{k_x}\sigma_{k_y}} = \frac{SWH^2_{swell}}{16\,\sigma_{k_x}\sigma_{k_y}}\ (m^4) \tag{50}$$

$S^0_{\widehat{Z_0}}$ and $S^0_{\widehat{\sigma_z}}$ may also depend on the ration of the spectral width of the swell spectrum ($\sim \sqrt{\sigma_{k_x}\sigma_{k_y}}$) to that of the MTF, which is roughly given by $k_0 \equiv \left(\frac{2}{\pi}\sqrt{\overline{\sigma_z}Z_{sat}}\right)^{-1}$, hence:

$$\eta \equiv \frac{\sqrt{\sigma_{k_x}\sigma_{k_y}}}{k_0} = \frac{2}{\pi}\sqrt{\sigma_{k_x}\sigma_{k_y}\overline{\sigma_z}Z_{sat}} = \frac{1}{\pi}\sqrt{\sigma_{k_x}\sigma_{k_y}SWH_{swell}Z_{sat}} \tag{51}$$

$\frac{S^0_{\widehat{Z_0}}}{\beta}$ and $\frac{S^0_{\widehat{\sigma_z}}}{\beta}$ are plotted on Figure 22 : (left) as functions of η ($S^0_{\widehat{Z_0}}$ and $S^0_{\widehat{\sigma_z}}$ in $\frac{m^2}{m^{-1}}$, β in $\frac{m^2}{m^{-2}}$). No dominating trend appears, but the values are more scattered towards lower η (corresponding to cases where the shape of the envelope spectrum come into play).

Also plotted on Figure 22 : (right) are the cutoff frequencies ratioed to k_0, $\frac{k^{-3dB}_{\widehat{Z_0}}}{k_0}$ and $\frac{k^{-3dB}_{\widehat{\sigma_z}}}{k_0}$, as functions of η. They show no significant trend when $\eta \gtrsim 1$, where the MTF cutoff dominates. For $\eta \lesssim 1$, they are determined by the combination of the envelope spectrum and the MTF, and are thus scattered, with a decreasing trend.

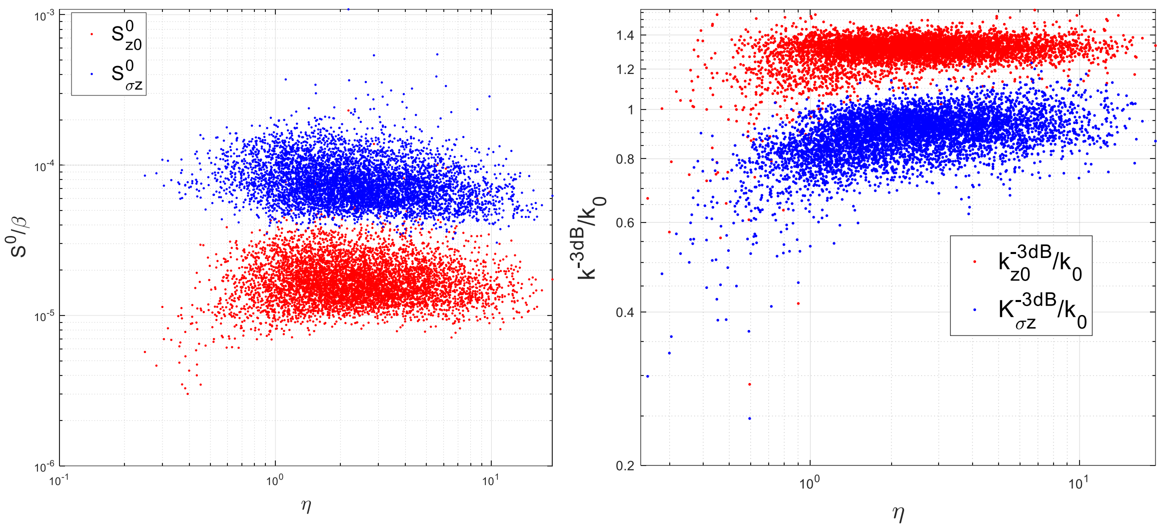

Figure 22 : low-frequency PSD (left) and frequency cutoff (right) as a function of parameter η, for 6000 sets of parameters (see text)

To derive the simplest empirical expressions for those parameters, we only consider the $\eta > 1$ domain (gathering 90% of the simulated cases), in which we have the following statistics:

$$\langle S^0_{\widehat{z_0}}\beta^{-1}\rangle = 1.67\ 10^{-5}\ \ m^{-1}$$

$$std\left(S^0_{\widehat{z_0}}\beta^{-1}\right) = 0.70\ 10^{-5}\ m^{-1}$$

$$\langle\frac{k^{-3dB}_{\widehat{z_0}}}{k_0}\rangle = 1.23$$

$$std\left(\frac{k^{-3dB}_{\widehat{z_0}}}{k_0}\right) = 0.06$$

$$\langle S^0_{\widehat{\sigma_z}}\beta^{-1}\rangle = 7.59\ 10^{-5}\ \ m^{-1}$$

$$std\left(S^0_{\widehat{\sigma_z}}\beta^{-1}\right) = 3.05\ 10^{-5}\ m^{-1}$$

$$\langle\frac{k^{-3dB}_{\widehat{\sigma_z}}}{k_0}\rangle = 0.84$$

$$std\left(\frac{k^{-3dB}_{\widehat{\sigma_z}}}{k_0}\right) = 0.06$$

(52)

From those statistics, simple expressions can be written:

$$S^0_{\widehat{Z_0}} \approx (1.7 \pm 0.7)10^{-5} m^{-1} \frac{SWH^2_{swell}}{16\, \sigma_{k_x} \sigma_{k_y}} \qquad (m^3)$$

$$k^{-3dB}_{\widehat{Z_0}} \approx (1.23 \pm 0.06) \frac{\pi}{2\sqrt{\overline{\sigma_z} Z_{sat}}} \qquad (m^{-1})$$

$$S^0_{\widehat{\sigma_z}} \approx (7.6 \pm 3.0)10^{-5} m^{-1} \frac{SWH^2_{swell}}{16\, \sigma_{k_x} \sigma_{k_y}} \qquad (m^3)$$

$$k^{-3dB}_{\widehat{\sigma_z}} \approx (0.84 \pm 0.06) \frac{\pi}{2\sqrt{\overline{\sigma_z} Z_{sat}}} \qquad (m^{-1})$$

(53)

The same relations are given bellow in more usual units according to $S(m^2 cpkm^{-1}) = \frac{2\pi}{1000} S\left(\frac{m^2}{rad}.m^{-1}\right)$

$$S^0_{\widehat{Z_0}} \approx (6.7 \pm 3)10^{-9} \frac{SWH^2_{swell}}{\sigma_{k_x} \sigma_{k_y}} \; (m^2 cpkm^{-1})$$

$$k^{-3dB}_{\widehat{Z_0}} \approx \frac{(615 \pm 30)}{\sqrt{SWH\, Z_{sat}}} \qquad (cpkm)$$

$$S^0_{\widehat{\sigma_z}} \approx (3.0 \pm 1.2)10^{-8} \frac{SWH^2_{swell}}{\sigma_{k_x} \sigma_{k_y}} \; (m^2 cpkm^{-1}) \qquad (m^2 cpkm^{-1})$$

$$k^{-3dB}_{\widehat{\sigma_z}} \approx \frac{(420 \pm 30)}{\sqrt{SWH\, Z_{sat}}} \qquad (cpkm)$$

Those simple fitting functions could be used to check wether the expected contribution of wave groups may, totally or partially explain observed spectral bumps.

Taking the median of $S^0_{\widehat{Z_0}}$ over the 6000 situations generated randomly (with no other physical meaning than plausible upper and lower values for each parameter) gives:

$$Median\left(S^0_{\widehat{Z_0}}\right) = (6.7 \pm 3)10^{-9}\, Median\left(\frac{SWH^2_{swell}}{\sigma_{k_x} \sigma_{k_y}}\right) = (6.7 \pm 3)10^{-9} \times 1.6\; 10^6$$
$$\simeq (1 \pm 0.5)10^{-2}\; m^2 cpkm^{-1}$$

Incidentally, this value coincides with the level of the plateau observed in LRM mode (Figure 1). The corresponding median cutoff frequency, $Median\left(k^{-3dB}_{\widehat{\sigma_z}}\right) \simeq 0.24\; cpkm$, is also compatible with the frequency of the "bump" in Figure 1 Average power spectral densities of the surface height typically observed in various altimetry modes, given that the -3dB level is not accessible because of the speckle noise.

Contrary to the spectra, whose magnitude is very sensitive to the swell parameters, the coherence is expected to remain essentially constant, except in case of small values of η. Coherence spectra obtained from ~1000 random parameters (including varying satellite altitude) are plotted on Figure 23, showing a variability of ± 0.1 at most. In simulated and, mostly, real data, other sources of $\widehat{z_0}$ and $\widehat{\sigma_z}$ fluctuations are expected to reduce the measured coherence. The magnitude of the coherence presented bellow should thus be considered as a maximum, reached in the absence of noise and other fluctuation mechanisms.

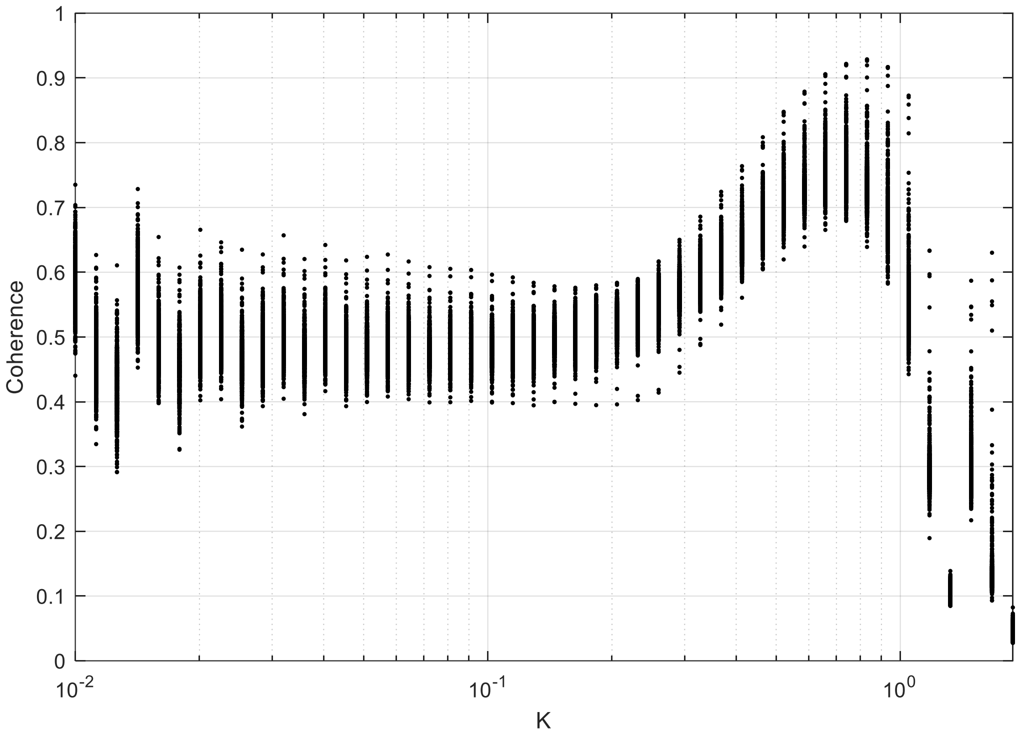

Figure 23 : coherence obtained through the model (eq. 47) for a wide range of sea state parameters and satellite altitude (see hereafter)

6. Comparison with Sentinel 6 data

As previously stressed, the general shape and magnitude of the spectral bumps seen in the data from various LRM altimeters are compatible with the model developed here. This is also the case for Sentinel 6 data (see Figure 24), with a bump maximum located at slightly lower wavenumber than in the case of Sentinel 3 (Figure 1), corresponding to the square-root of the ration of their altitudes (eq. (13)), $\sqrt{800/1300} = 0.78$.

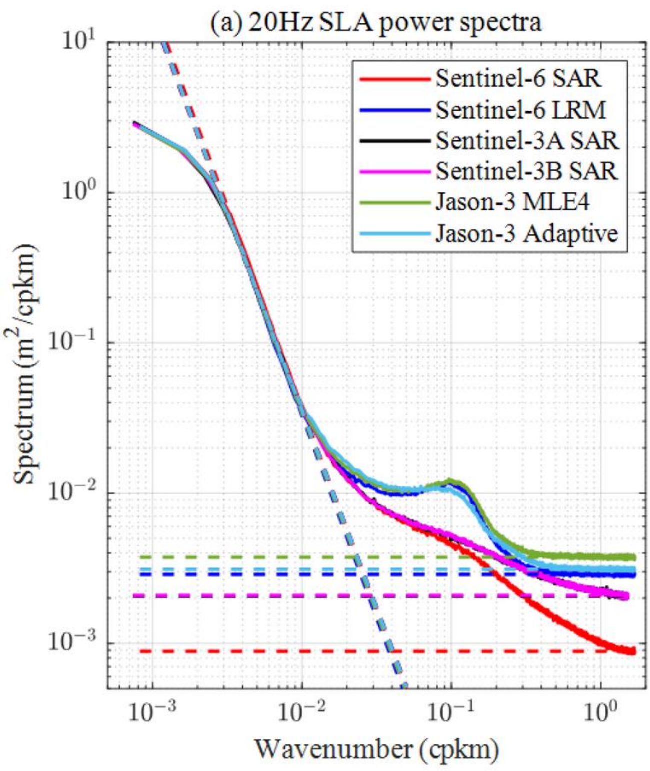

Figure 24 : S6 SSH spectrum from https://www.mdpi.com/2072-4292/15/1/12

Although those spectra are compatible with a significant contribution of SWH variations, especially (but not necessarily only) from wave groups, this can hardly be demonstrated from those data alone. Other mechanisms could contribute to- or even dominate SSH variations and they would also fulfill the frequency cutoff related to the instrument footprint. Unfortunately, analyzing quantitatively the bump magnitude requires a knowledge of the swell spectrum (SWH and spread in wavenumber and azimuth, at least).

SWIM data, offering both altimetric and wave spectra estimated parameters, would offer a nice opportunity to test the model and to derive the relative magnitude of wave groups contribution.

Before going into this demanding work, S6 LRM data can be very simply used to perform a first testing based on the shape of SSH and SWH spectra and their coherence.

As previously underlined, coherence spectrum provides a robust and straightforward way for checking that a relation between SWH and SSH variations does exist, especially in the vicinity of the spectral bump.

Figure 25 shows SWH and SHH spectra (top) and coherence (bottom), obtained from S6 data (continuous lines), analytical model (dashed lines) and synthetic data (stars). While the sea state is not known (except estimated SWH, which is not enough to constrain the models), the spectra have be scaled to make the magnitude of the modelled SWH bump coincide with that of the observed one.

The numerical simulation nicely reproduces the shape of the SWH spectrum in the bump region, including a "secondary bump" related to an oscillation of the FTM. The SSH spectrum is not so correctly simulated, the plateau level being underestimated by a factor ~2. Again, S6 data exhibit secondary bumps, as qualitatively expected from the MTF shape.

The coherence spectrum exhibits a maximum coinciding with that seen in simulated data ($\simeq 0.55$ @ $K \simeq 0.5$). It decreases faster than the simulated curve towards low frequencies, probably due to fluctuations of SSH not (or less) correlated to SWH. Towards higher frequencies, the observed coherence remains significant, perhaps through correlated noise in retrieved SSH and SWH.

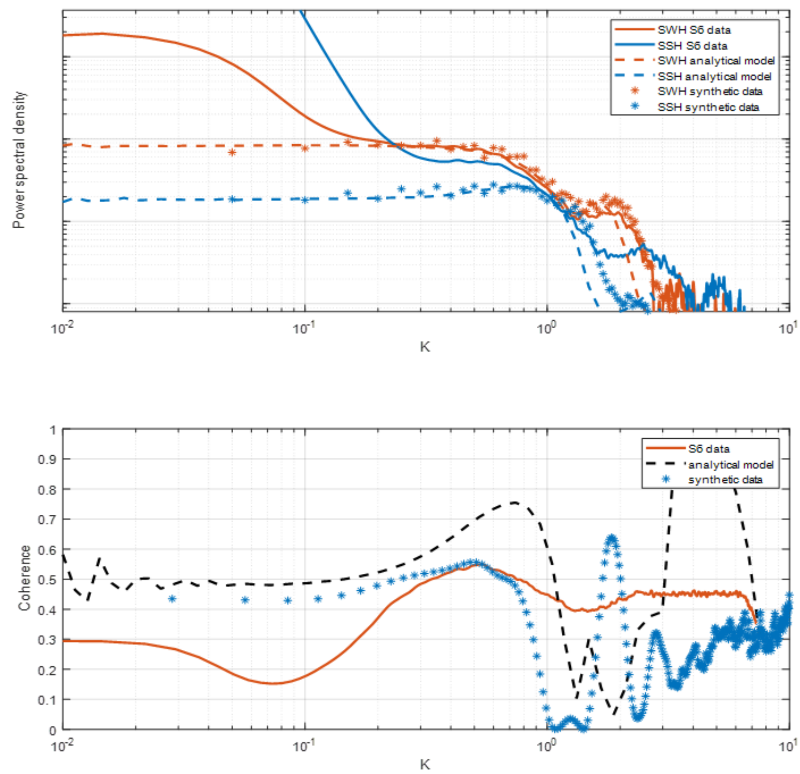

Figure 25 : SSH and SWH spectral shapes from S6 data, simulated data and semi-analytical model (top). Corresponding coherence spectra (bottom).

The observed magnitude of the coherence in the bump confirms that the process modelled in this work (SSH fluctuations induced by SWH variations) significantly contributes to the bump, even if it does not exclude other sources of fluctuations. Another question is the part of SWH fluctuations due to the envelope spectrum, as SWH variations from other origin could also contribute. Because the envelope spectrum is wide and fairly isotropic, it tends to completely “fill” the bidimensional MTF in most swell cases, giving rise to spectral bump and coherence very constant in shape. SWH variations resulting from other processes (current, bathymetry…) would probably be more directional and narrow-banded, which should lead to significant variations in the bump and coherence shape (the cutoff frequency being reached only for along-track variations). the variability of the bump and coherence shape could be studied in order to discriminate between wave groups and other sources of SWH variations.